Engineering Structures 265 (2022) 114400

Contents lists available at ScienceDirect

Engineering Structures

journal homepage: www.elsevier.com/locate/engstruct

Effect of stress reversals on fatigue life evaluation of OSD considering the transverse distribution of vehicle loads

Shengquan Zou [a], Ran Cao [a,b], Lu Deng [a,b,*], Wei Wang [a,b]

[a] College of Civil Engineering, Hunan Univ., Changsha, China
[b] Key Laboratory of Damage Diagnosis for Engineering Structures of Hunan Province, Hunan Univ., Changsha, China

ARTICLE INFO

Keywords:
Orthotropic steel deck
Lightweight composite deck
Fatigue life evaluation
Finite element
Stress reversal
Vehicle transverse location

ABSTRACT

The effect of stress reversals, generated by vehicles passing the bridge deck in sequence from different transverse locations, has been underestimated or even ignored in the fatigue life evaluation of orthotropic steel decks (OSDs), which may result in an overestimated fatigue life of the whole bridge. In this paper, four distribution patterns of vehicle transverse locations were considered and the effect of stress reversals on the fatigue evaluation of a conventional OSD (COSD) and a lightweight composite deck (LWCD) was investigated from infinite-life and finite-life perspectives based on finite element analysis. The results show that the maximum stress range could be underestimated by over 40% if the most unfavorable stress reversal is underestimated. A convenient and efficient vehicle loading scheme was proposed to determine the accurate maximum stress range for the infinite fatigue life evaluation of OSDs. Besides, the stress reversals are found to have a significant effect on the finite fatigue life evaluation of both the COSD and the LWCD, and the fatigue life of COSDs could be overestimated by 95% if the stress reversals are ignored. Nevertheless, the effect of stress reversals on the finite fatigue life evaluation of the LWCD is much less than that of the COSD, which indicates a better anti-fatigue performance of the LWCD over the COSD. In addition, the stress reversals induced by overloaded trucks have a significant effect on the fatigue performance of OSDs. The results from the study can provide some references for the fatigue design and evaluation of OSD systems.

1. Introduction

Orthotropic steel decks (OSDs) have been widely employed in medium and long-span bridges around the world due to their outstanding advantages, such as suitability for standardization and prefabrication, longer-term durability, and lower life-cycle cost [1–3]. Typically, the thickness of steel plates in an OSD is strictly limited to reduce its self-weight, and thus the local stiffness of the OSD is usually insufficient, resulting in fatigue cracking when subjected to ever-increasing traffic loads [4–6]. Over the past few decades, fatigue cracking has become an increasingly prevalent phenomenon in OSDs [7–9]. In order to address the fatigue problem of the conventional OSD (COSD), a novel OSD system, i.e., the lightweight composite deck (LWCD) using ultra-high performance concrete (UHPC), was proposed by Shao et al. [10] and has been applied to many bridges in recent years [11]. However, it is still difficult to accurately predict the fatigue life of OSDs because of their complicated geometries and mechanisms of load transfer [12–14].

In general, the design of OSDs is controlled by the fatigue limit state rather than the ultimate limit state, and the fatigue life evaluation of the local components in OSDs is typically dominated by stress ranges induced by traffic loads [15]. In practice, the fatigue design and evaluation of OSDs are conducted from the perspectives of infinite and finite fatigue life [16].

For a steel component with an infinite fatigue life, it is crucial to check whether the maximum stress range experienced by the fatigue-prone details in the steel component is less than the corresponding constant amplitude fatigue limit (CAFL) [16]. Since the stresses experienced by fatigue-prone details in OSDs are highly sensitive to the location of vehicle wheels [17], the fatigue-prone details may be alternately subjected to tensile and compressive stresses when trucks travel across the bridge deck in sequence from different transverse locations, resulting in the fatigue-prone details suffering stress reversals [18]. Therefore, the most unfavorable stress reversal experienced by fatigue-prone details should be considered when determining the maximum

* Corresponding author at: Key Laboratory of Damage Diagnosis for Engineering Structures of Hunan Province, Hunan University, Changsha, Hunan 410082, China.

E-mail address: denglu@hnu.edu.cn (L. Deng).

https://doi.org/10.1016/j.engstruct.2022.114400
Received 30 December 2021; Received in revised form 9 April 2022; Accepted 8 May 2022
Available online 3 June 2022

stress range used to evaluate the infinite fatigue life of OSDs [19]. In other words, the maximum and minimum stresses should be determined separately by a fatigue design truck traveling along the unfavorable paths [20]. In general, the influence surface method can be used to determine the accurate maximum stress range [21], but it is poor in computational efficiency. To minimize computing costs, a simplified loading method has been commonly used to calculate the maximum stress range of critical fatigue-prone details in OSDs, in which the fatigue design load is applied along three typical wheel paths (TTWP), i.e., over-rib, riding-rib, and between-rib [12,22]. However, it was found that the maximum stress range of some fatigue-prone details measured by the field test is significantly greater than the result calculated by TTWP [23], which was also confirmed by Li et al. [24] based on the finite element (FE) analysis. Hence, the most unfavorable stress reversal experienced by these fatigue-prone details cannot be obtained using TTWP, which may result in an underestimated maximum stress range and an inaccurate estimation of the infinite fatigue life of OSDs. Therefore, a convenient and efficient vehicle loading scheme is required to determine the accurate maximum stress range of fatigue-prone details in OSDs under the action of vehicle loads for the infinite fatigue life evaluation.

On the other hand, the finite fatigue life of a steel component is generally evaluated based on the corresponding *S-N* curve and Miner's rule [25–26]. It was found that the stress responses of weld joints in OSDs and their fatigue lives can be affected by the transverse location of vehicles [15,27]. The fatigue damage would be estimated incorrectly when the transverse location of vehicles is ignored, resulting in an inappropriate implementation of bridge design and management [28]. Multi-path models are recommended in many bridge codes, including the BS 5400 [29] and Eurocode 1 [21], to account for the effect of vehicle transverse positions on the fatigue evaluation of OSDs. Besides, previous studies have shown that the distribution of vehicle transverse locations recommended by the bridge code may be unsuitable for the local truck traffic [12,30]. However, the stress ranges of fatigue-prone details in OSDs used to evaluate the finite fatigue life are obtained separately when the fatigue design truck travels across the bridge from each recommended transverse location. As a result, the effect of stress reversals generated by vehicles passing the bridge deck in sequence from different transverse locations is ignored in the process of fatigue damage calculation, which may result in an underestimated equivalent stress range of fatigue-prone details and thus an overestimated finite fatigue life of OSDs. Besides, the fatigue damage induced by increasing overloaded vehicles may also be underestimated if stress reversals are not considered.

This paper aims to investigate the effect of stress reversals on the fatigue life evaluation of OSDs, including the COSD and the LWCD, considering the transverse distribution of vehicle loads. Based on a super-span cable-stayed bridge, FE models of the COSD and the LWCD were established. Six fatigue-prone details in these two OSD systems were considered. The maximum stress ranges of these critical details under the action of fatigue design loads were calculated with the influence surface method, and the results were compared with those obtained from TTWP. More importantly, a convenient and efficient vehicle loading scheme was proposed to determine the accurate maximum stress range of fatigue-prone details in OSDs. Based on the proposed loading scheme, the effects of stress reversals on the finite fatigue life of fatigue-prone details in these two OSD systems were investigated, considering four distribution patterns of vehicle transverse locations and four overloading rates. The results from the study can provide important insights for the fatigue design and evaluation of OSD systems.

2. Bridge deck systems

2.1. Information of bridge decks

In this paper, two different OSD systems, including the COSD and the LWCD, were selected to investigate the effect of stress reversals on the fatigue life evaluation of steel components in OSDs, considering various transverse distributions of vehicle loads. Based on a super-long span cable-stayed bridge design [31], the cross-sections of these two considered OSD systems are shown in Fig. 1. In the COSD system, the bridge deck is covered by a 55-mm-thick double-layer epoxy asphalt overlay and supported by 8-mm-thick U-ribs with a transverse spacing of 0.6 m and 12-mm-thick crossbeams with a longitudinal spacing of 4.0 m. The LWCD system was first proposed by Shao et al. [10] to improve the fatigue performance of COSDs, in which a 50-mm-thick UHPC layer is poured on the deck plate and then the UHPC layer is covered by a wearing course with a thickness of 10–15 mm. The short studs with a spacing of 0.2 m are welded on the deck plate to strengthen the connection between the deck plate and the UHPC layer [32]. It should be noted that the thickness of deck plates in COSDs is generally designed to be no less than 14 mm, while in LWCDs it can be reduced to 12 mm due to the UHPC layer contributing to significantly improving the local stiffness of the bridge deck and evenly distributing local wheel loads [31]. To better quantify the comparison results between these two systems in terms of the fatigue performance, the thickness of deck plates in both the COSD and the LWCD was set as 12 mm in this paper. Besides, the effect of the wearing layer in the LWCD was ignored and the thickness of asphalt layers in the COSD was set to be the same as the UHPC layer.

2.2. FE models of bridge decks

According to previous studies, the influence area of wheel loads on fatigue-prone details in OSDs is quite local [19], and the accurate stress ranges of fatigue-prone details of interest can be obtained through numerical simulations using a local FE model [33]. In this paper, the local girder segmental FE models of the COSD and the LWCD were built using the commercial software ANSYS, as shown in Fig. 2. Considering that the steel component generally remains linear-elastic in the fatigue limit state [34] and the peak stresses experienced by components in the OSD system under the action of vehicle loads have been confirmed to be far below the corresponding ultimate strengths [10], the FE models in the present study were assumed to be kept in the linear-elastic stage. All steel plates, including the deck plate, U-ribs, and crossbeams, were modeled with the higher-order element SHELL181 (Young's modulus = 210.0 GPa, Poisson's ratio = 0.3). The UHPC layer in the LWCD was simulated with the solid element SOLID185 (Young's modulus = 42.6 GPa, Poisson's ratio = 0.2), and the short studs were simulated with the beam element BEAM189 with the same mechanical properties as the steel plates. It should be pointed out that the role of asphalt overlay in the COSD was considered through the dispersion effect on wheel loads. Besides, the weld in welding joints was omitted in the present FE model to improve computing efficiency, which has been confirmed to be acceptable by the International Institute of Welding (IIW) [16]. It has been found by Li et al. [24] that the error in stresses obtained from such a simplified FE model is about 1% if the mesh size of elements is less than 5 mm. Additionally, it is reasonable to mesh the higher-order element near the hot spot with a size of $t \times t$ (t = the thickness of the steel plate at the weld toe) [35]. In this paper, the mesh size near the fatigue-prone details under consideration was set as 0.5 t and the mesh density of elements far away from these fatigue-prone details decreased gradually. Overall, the FE model of the LWCD consists of 400,596 elements and 449,784 nodes with a minimum mesh size of 4 mm.

In the present FE model, the X-axis, Y-axis, and Z-axis were defined as the transversal, vertical, and longitudinal directions along the bridge deck, respectively, as shown in Fig. 2**(a)**. The degrees of freedom (DOFs) of the longitudinal translation, as well as the transversal and vertical rotations of nodes at both ends of the FE model, were constrained, except for those of the nodes at the end-crossbeams. The DOFs of the transversal translation, as well as the vertical and longitudinal rotations of nodes at both sides of the present model, were constrained, and the DOFs of the vertical translation of nodes at the bottom of the crossbeams

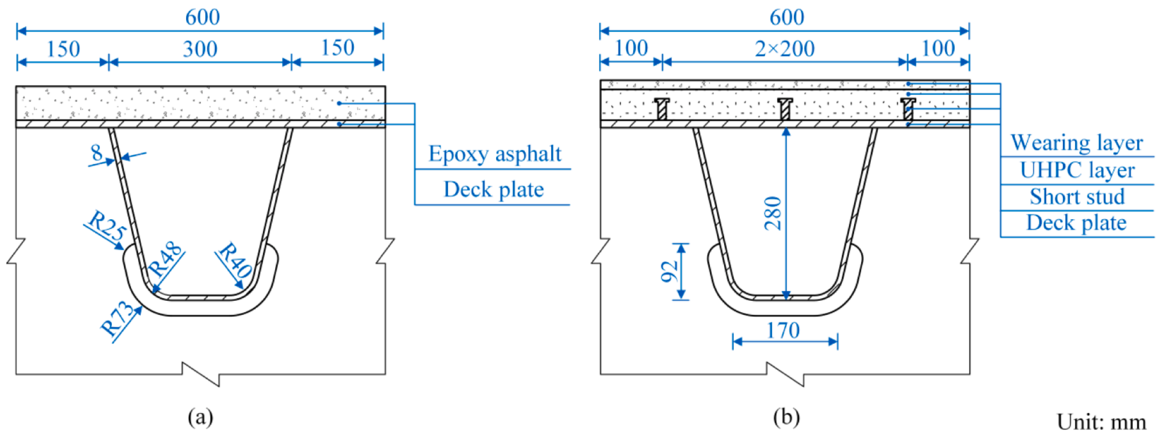

Fig. 1. Cross-sectional details of OSD systems: (a) COSD; (b) LWCD.

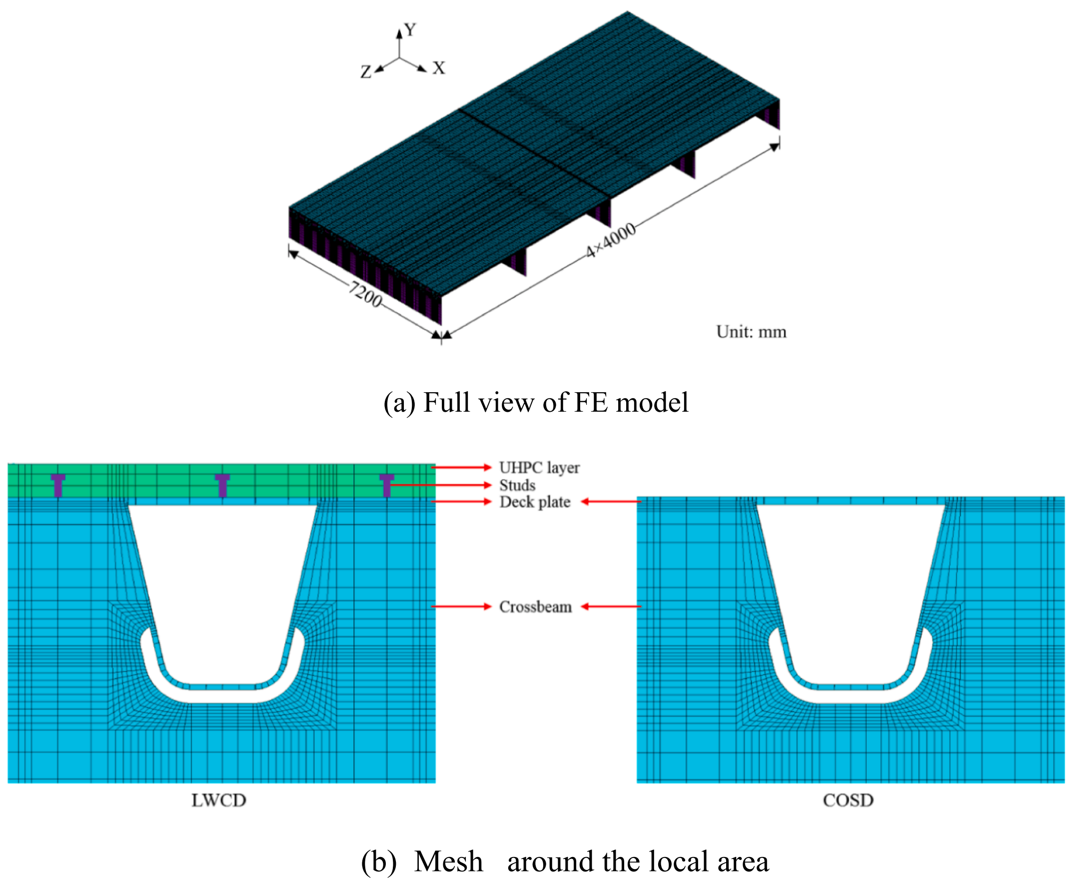

Fig. 2. Local FE models of OSDs.

were also constrained. Besides, the coupling effect between the upper of the short studs and the UHPC layer was considered, and the coincident nodes between the short studs and the deck plate were coupled. In addition, as the bond-slip effect on the interface between the deck plate and the UHPC layer rarely affects the stress of fatigue-prone details in the LWCD [24], the horizontal shear-bond between them was ignored in the FE model, and only DOFs of the vertical translation of nodes at the contact surface between them were coupled [36]. Based on the Saint Venant principle, the calculated results in this paper would be little affected by the boundary condition of the FE model as the fatigue-prone details under consideration are far away from the boundaries [23]. The accuracy of the local FE model of the girder segment of the LWCD has also been validated based on the design documents and experimental tests by Shao et al. [31].

3. Fatigue-prone details

Zhang et al. [6] summarized over seventeen types of fatigue cracks observed in the OSD system due to different crisscrossed steel plates and dense welds. Based on their study, six typical fatigue-prone details were considered in this paper and were illustrated in Fig. 3, including the transverse splice weld in deck plate (D1), the rib-to-deck weld in deck plate (D2), the rib-to-deck weld in rib (D3), the rib-to-crossbeam weld in the web of rib (D4), the rib-to-crossbeam weld in rib wall at cutout (D5),

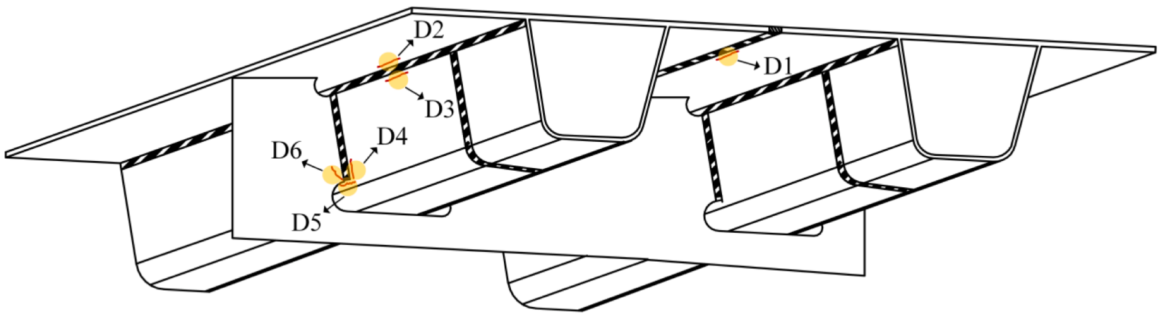

Fig. 3. Fatigue-prone details under consideration.

and the rib-to-crossbeam weld in crossbeam (D6).

Due to the high cost of fatigue tests, numerical methods for fatigue evaluation have been developed based on fatigue test data. The nominal and hot spot stress methods are two commonly-used methods based on the *S-N* curve and Miner's rule [15]. The hot spot stress method is generally employed to obtain the local stress of complex structures, especially the welded joint, and the hot spot stress at welded details of interest can be determined through the surface stress extrapolation technique based on the stresses at reference points obtained from FE models [37]. According to the IIW [16], the types of hot spots are shown in Fig. 4, including Type a (weld toe on the plate surface) and Type b (weld toe at the plate edge), and the corresponding stress evaluation paths for welded details in the shell element model are illustrated in Fig. 5.

In this paper, hot spot stresses of fatigue-prone details under consideration were determined as below. For the fatigue-prone detail of type "a" hot spot modeled with higher-order elements, the hot stress was obtained through linear extrapolation based on the node stresses of two reference points, as calculated in Eq. (1) [16]:

$$\sigma_{\text{hot}} = 1.5 \cdot \sigma_{0.5 \cdot t} - 0.5 \cdot \sigma_{1.5 \cdot t} \tag{1}$$

where σ_{hot} is the hot stress; $\sigma_{0.5t}$ and $\sigma_{1.5t}$ are the node stresses of reference points with a distance of 0.5 *t* and 1.5 *t* away from the hot spot, respectively; and *t* is the thickness of steel plate.

For the fatigue-prone detail of type "b" hot spot meshed with a mesh size of not more than 4 mm, the hot stress was obtained through quadratic extrapolation based on the node stresses of three reference points, as calculated in Eq. (2) [16]:

$$\sigma_{\text{hot}} = 3 \cdot \sigma_{4\text{mm}} - 3 \cdot \sigma_{8\text{mm}} + \sigma_{12\text{mm}} \tag{2}$$

where $\sigma_{4\text{mm}}$, $\sigma_{8\text{mm}}$, and $\sigma_{12\text{mm}}$ are the node stresses of reference points with a distance of 4, 8, and 12 mm away from the hot spot, respectively.

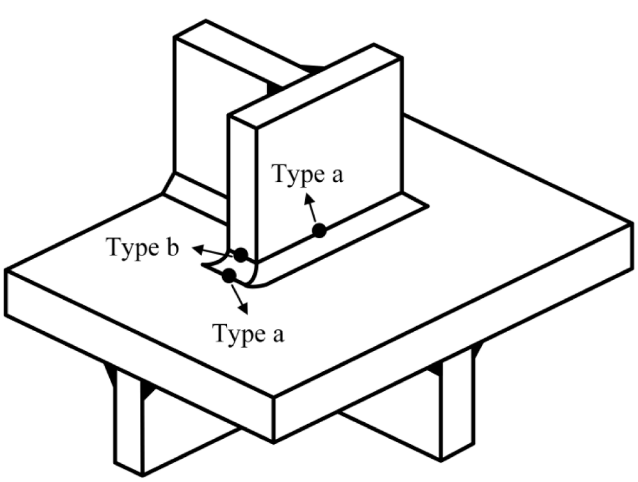

Fig. 4. Types of hot spots.

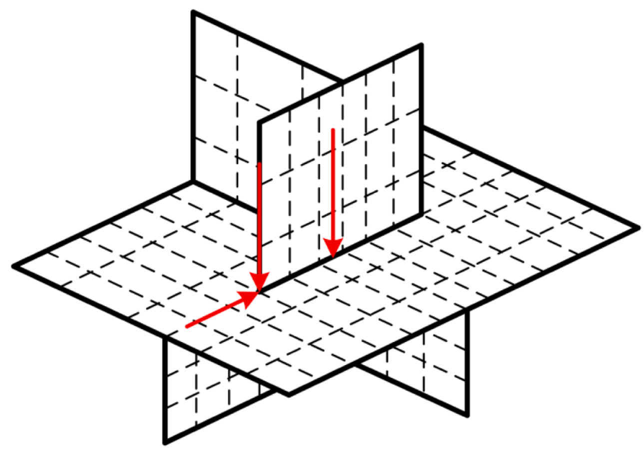

Fig. 5. Stress evaluation paths for welded details.

The information of fatigue-prone details under consideration in this paper is listed in Table 1, where the stress of detail D1 was obtained using the nominal stress method, while the stresses of other fatigue-prone details were obtained through the hot spot method. In addition, the fatigue-prone details under consideration were classified according to Eurocode 3 [20].

4. Fatigue design loads

4.1. Load model

The Fatigue Load Model 3 specified in the Chinese design specification for steel bridges [38] was adopted as the fatigue design loads in this paper, as shown in Fig. 6, in which the contact area between tires

Table 1
Classifications and parameters of details under consideration.

Detail	Stress type	Type of hot spot	Stress direction	$\Delta\sigma_C$ (MPa)	$\Delta\sigma_D$ (MPa)	$\Delta\sigma_L$ (MPa)
D1	Nominal	—	S_X	90	66.3	36.4
D2	Hot spot	a	S_X	71	52.3	28.7
D3	Hot spot	a	$S_{Y'}/S_{Y''}$	71	52.3	28.7
D4	Hot spot	a	S_Z	80	59.0	32.4
D5	Hot spot	a	$S_{Y'}/S_{Y''}$	80	59.0	32.4
D6	Hot spot	b	S_1	80	59.0	32.4

Note: (a) the stress direction was shown in Fig. 7 and S1 is the principal stress; (b) $\Delta\sigma_C$ is the detail category of fatigue-prone details (2×10^6 cycles); $\Delta\sigma_D$ is the constant amplitude fatigue limit (CAFL) (5×10^6 cycles), and$\Delta\sigma_D = 0.737\Delta\sigma_C$; $\Delta\sigma_L$ is the cut-off limit (1×10^8 cycles), and$\Delta\sigma_L = 0.549\Delta\sigma_D$. More details can be found in Eurocode 3 [25].

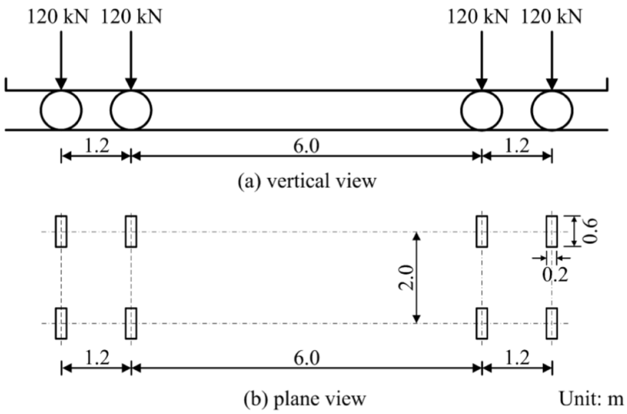

Fig. 6. Fatigue load model.

and the pavement was defined as 200 × 600 mm (longitudinal direction × transverse direction). A dynamic factor of 0.15 specified in the bridge code for fatigue design loads was adopted to consider the dynamic effect of vehicle loads on the results. Since the stresses of fatigue-prone details in the COSD and the LWCD are mainly affected by local wheel loads applied close to these fatigue-prone details [12,23], only two rear axles (120 kN + 120 kN) with a spacing of 1.2 m were used to obtain the stress influence surfaces of fatigue-prone details. Based on previous studies [15], the critical stresses of fatigue-prone details were found to be controlled by a single truck event. Hence, cases of simultaneous multi-vehicle crossings on the bridge deck were not considered in this paper.

4.2. Loading scenarios

As previously stated, a simplified loading method using TTWP has been widely used to calculate the maximum stress range of fatigue-prone details of interest in OSDs to enhance computational efficiency. Fig. 7 illustrates its loading scenarios, where the fatigue design loads are applied along three typical loading paths, i.e., over-rib, riding-rib, and between-rib. To determine the most unfavorable stress reversal experienced by fatigue-prone details of interest, the stress responses of these details were captured using the influence surface method [21], and the loading scheme is shown in Fig. 8. In particular, taking the center of the lateral wheels as the reference point, the wheel loads were applied from Crossbeam $2^{\#}$ to Crossbeam $4^{\#}$ with a step length of 0.10 m in the Z-direction and from U-rib $1^{\#}$ to U-rib $7^{\#}$ with a step length of 0.05 m in the X-direction. Eventually, a total of 96 (in Z-direction) × 73 (in X-direction) load steps were performed, which can be interpreted as 73 longitudinal wheel loading paths with different transverse locations. It can be found from Fig. 8 that the TTWP are three specific loading schemes included in the loading scenarios of the influence surface method.

5. Calculation results and discussion

5.1. Infinite fatigue life evaluation

Theoretically, the steel component is expected to have an infinite fatigue life if the experienced maximum stress range is less than the corresponding CAFL [34]. The requirement for an infinite fatigue life of steel components can be described as [20]:

$$\gamma_{Ff}\cdot\lambda\cdot\Delta\sigma_p \leqslant \Delta\sigma_C/\gamma_{Mf} \tag{3}$$

where γ_{Ff} is the partial factor for fatigue stress ranges, adopting a value of 1.0 [20]; γ_{Mf} is the partial factor for fatigue strength, which was taken as 1.0 considering that the fatigue cracking in OSDs can be regularly inspected [18,25]; $\Delta\sigma_p$ is the maximum stress range induced by fatigue design loads considering the dynamic impact factor; $\Delta\sigma_C$ is the CAFL at the number of cycles $N_C = 2 \times 10^6$, as listed in Table 1; and λ is the damage equivalence factor, calculated as $\lambda = \lambda_1 \bullet \lambda_2 \bullet \lambda_3 \bullet \lambda_4$ and should not exceed $\lambda_{\max}$, in which $\lambda_{\max}$ was taken as 2.5 and 1.8 for fatigue-prone details at the midspan and the support, respectively, and λ_i ($i = 1$, 2, 3, and 4) is the factor accounting for the effect of the length of the bridge span, traffic volume, design life, and traffic on other lanes, respectively. It should be emphasized that the modified factors in Eq. (3) do not take into account the effect of stress reversals on the fatigue life of fatigue-prone details.

According to Eq. (3), obtaining the accurate maximum stress range induced by traffic loads is the key to evaluating the infinite fatigue life of steel components in OSDs. In this section, the stress influence surfaces of fatigue-prone details under consideration in the COSD and the LWCD were obtained through numerical simulations according to the influence surface method introduced in Fig. 8, and the results are shown in Fig. 9. It is worth noting that these fatigue-prone details are located near U-rib $4^{\#}$ shown in Fig. 8. Specifically, details D1, D2, and D3 were selected from the welds located at the most unfavorable section of the interior span between Crossbeam 3# and 4#. While details D4, D5, and D6 were chosen from Crossbeam $3^{\#}$.

It can be seen from Fig. 9 that the stress of each fatigue-prone detail in both the COSD and LWCD occurs in a local area and that the stress fluctuates greatly with the variation of the location of wheel loads when wheel loads are around the fatigue-prone details. Taking detail D3 in the COSD for example, the stress greater than 10 MPa is only generated by the wheel loads applied on the area of 0.60 m < X less than 1.10 m or 1.55 m < X less than 3.15 m and −3.50 m < Z < -0.40 m, and the maximum and minimum stresses occur when the wheel loads are applied at X = 2.05 m and 2.35 m, respectively. Besides, for fatigue-

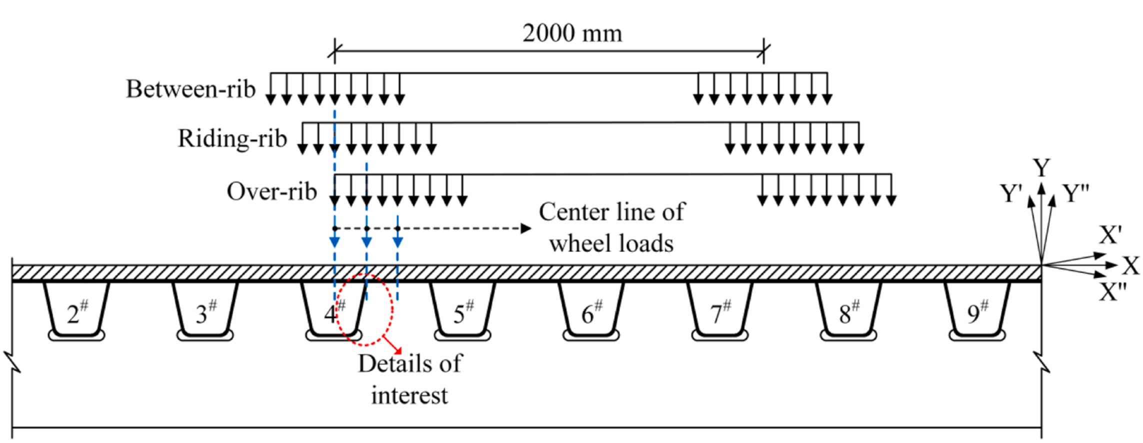

Fig. 7. Loading scenarios of TTWP.

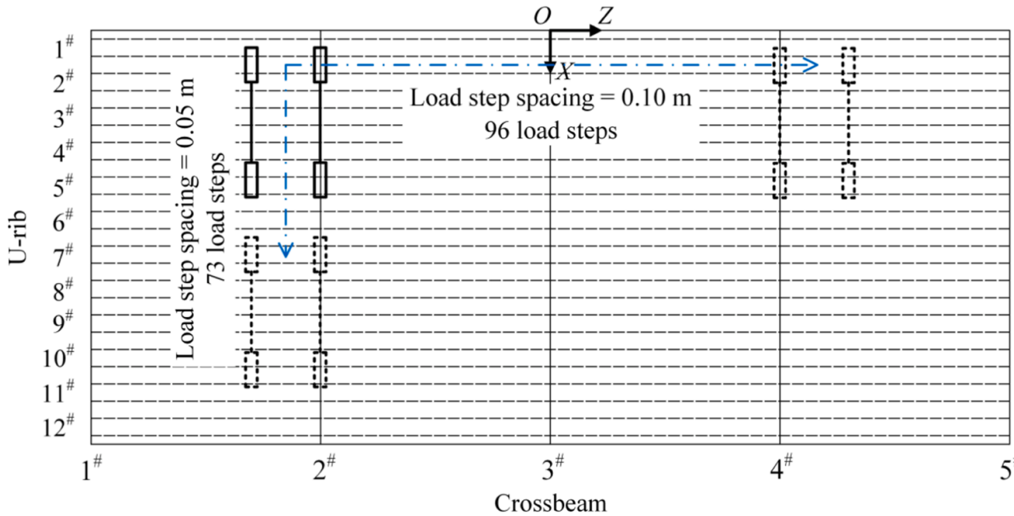

Fig. 8. Loading scenarios of influence surface method.

prone details in the COSD, the transverse distance between the wheel loads generating the maximum and minimum stresses ranges from 0.30 m to 0.70 m, while it ranges from 0.45 m to 0.85 m for fatigue-prone details in the LWCD. These findings suggest that the fatigue-prone details in both the COSD and the LWCD may experience stress reversals when the wheel loads are applied along with different transverse locations in succession and that the most unfavorable stress reversal can be generated by vehicles passing the bridge deck in sequence from two critical transverse locations in the same traffic lane. In addition, the stress variation trend of the fatigue-prone details near the deck plate in the LWCD (i.e., details D1, D2, and D3) is relatively smoother than that in the COSD, indicating that the local tire force in the LWCD is more evenly-distributed due to the UHPC layer.

The maximum and minimum stresses (i.e., S^1_{max} and S^1_{min}) of fatigue-prone details in the COSD and the LWCD under the action of fatigue design loads were extracted from the stress influence surfaces, and then the maximum stress ranges (SR^1) were determined, as illustrated in Fig. 10. The maximum and minimum stresses (i.e., S^2_{max} and S^2_{min}), as well as the corresponding maximum stress ranges (SR^2), obtained through the TTWP method (as illustrated in Fig. 7**)**, were also plotted in Fig. 10 for comparison. It can be found from Fig. 10 that although the most unfavorable stress experienced by the fatigue-prone details of interest can be accurately calculated by TTWP, the accurate maximum and minimum stresses of these fatigue-prone details (except detail D2) cannot be captured concurrently, resulting in a significantly underestimated maximum stress range. Taking detail D4 in the LWCD for example, the maximum stress calculated by TTWP is 71.3 MPa, which is close to the exact value (72.7 MPa) obtained using the influence surface method. However, the minimum stress (-2.0 MPa) obtained from the former method is significantly lower than the value (-36.5 MPa) obtained from the latter method. For detail D5 in the COSD, the deviation of the minimum stress obtained using the TTWP method even reaches 74.0 MPa, and thus the maximum stress range would be underestimated by about 42%, potentially leading to a misjudgment of infinite fatigue life evaluation of fatigue-prone details. In addition, the stress response of each fatigue-prone detail in the LWCD is much less than that of the COSD. In particular, the maximum stress range of detail D2 in the LWCD is reduced by more than 90.0 MPa when compared to that of the COSD, and the reduction ratio reaches 73%, which indicates that the LWCD can significantly enhance the fatigue performance of OSDs.

In practice, a general reduction factor of 0.75 is adopted in the AASHTO bridge design specifications [34] to account for the low probability event that two trucks travel across the bridge one after another from two critical transverse locations. However, there is no provision in this code that the maximum cycle of stress range generated by two trucks must be taken into account. In general, the most unfavorable stress range caused by a single fatigue design truck is used. The calculation results under these two conditions are illustrated in Fig. 11 for comparison, including the maximum stress range obtained from the stress influence surface considering a reduction factor of 0.75 (i.e., Condition (1)') and that induced by a single fatigue design truck traveling from the most unfavorable transverse path (i.e., Condition (2)'). It can be seen from Fig. 11 that the maximum stress range of several fatigue-prone details obtained under Condition (1)' is still much larger than that obtained under Condition (2)', which indicates that the effect of the most unfavorable stress reversal cannot be ignored.

It should be noted that it is acceptable for the verification of infinite fatigue life that the frequency of stress ranges exceeding the CAFL is less than 0.01 percent [15]. However, the results in Fig. 9 have confirmed that the transverse distance between the wheel loads generating the maximum tensile and compressive stresses of the fatigue-prone details in OSDs ranges from 0.30 m to 0.85 m. Besides, the measured distribution of vehicle transverse locations indicated that the frequency of vehicles transversely offsetting the lane centerline by 0.6 m can reach 5% [39], and the frequency for heavy trucks may also be over 3% [40]. As a result, the probability of trucks traveling across the bridge deck sequentially from different transverse locations and thus inducing the stress ranges of fatigue-prone details in OSDs that exceed the CAFL is likely to be much higher than 0.01 percent. Therefore, the most unfavorable stress reversal generated by vehicles passing the bridge from two specific transverse locations should be considered in the infinite fatigue life evaluation of fatigue-prone details in OSDs.

Although the accurate maximum stress range of fatigue-prone details can be determined using the influence surface method, the process is time-consuming as thousands of load steps are required to be calculated. It was found that the wheel loads are mainly shared by three stiffeners in the transverse direction, including the stiffener below the tire and two adjacent stiffeners [15]. Besides, it can be found from Fig. 9 that the transverse locations of wheel loads inducing the maximum and minimum stresses of each fatigue-prone detail are typically distributed within two U-ribs near the fatigue-prone detail. Therefore, a convenient and efficient loading method was proposed to accurately capture both the maximum and minimum stresses of fatigue-prone details under the action of vehicle loads in this paper, as illustrated in Fig. 12. The proposed loading scheme consists of nine typical wheel loading paths located within 1.2 m (namely, the spacing of two U-ribs) around the fatigue-prone detail of interest, which can still be classified into three categories, i.e., over-rib, riding-rib, and between-rib.

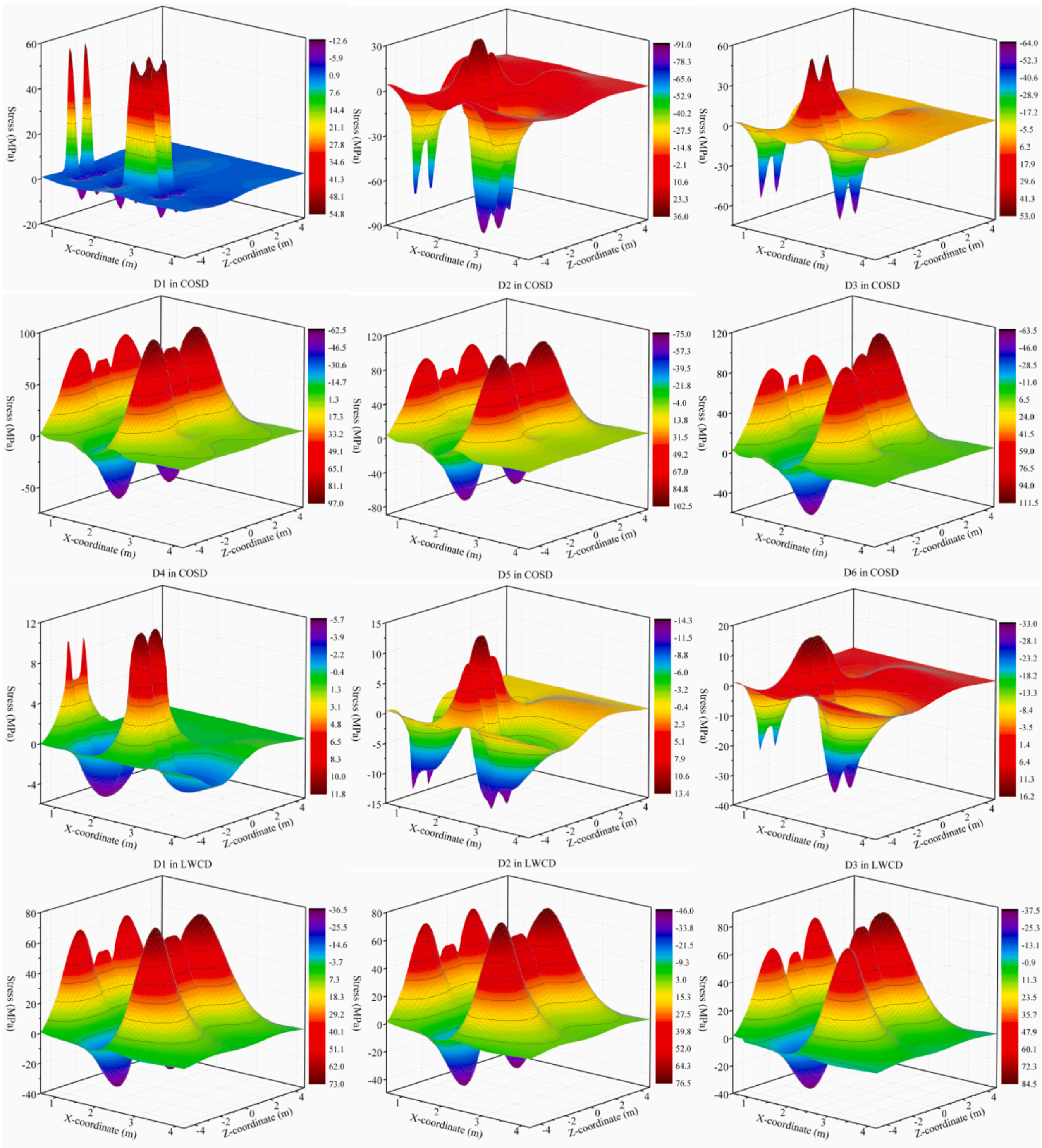

Fig. 9. Stress influence surfaces of fatigue-prone details under consideration.

Although the proposed loading scheme requires three times the computation cost of the TTWP method, it is still more efficient than the influence surface method. As shown in Fig. 13, the results obtained using the influence surface method (denoted with the superscript of “1″) were compared with those obtained through the proposed loading scheme (denoted with the superscript of “3”). The comparison results in Fig. 13 reveal that the maximum and minimum stresses of each fatigue-prone detail obtained from these two methods are almost identical and that the maximum error between the maximum stress ranges obtained from these two methods is less than 3%. This indicates that it is efficient to determine the maximum stress range of fatigue-prone details in the COSD and the LWCD based on the proposed loading scheme.

5.2. Finite fatigue life evaluation

In comparison to the infinite-life fatigue design, the finite-life fatigue design may be a more economical choice for bridges with limited design service life [34]. According to the previously calculated results, both the COSD and the LWCD contain fatigue-prone details that do not meet the requirement of infinite fatigue life. Therefore, it is necessary to further evaluate the finite fatigue life of these fatigue-prone details. Based on the *S-N* curve and the Miner’s rule [25–26], the accumulated fatigue damage can be calculated as follows:

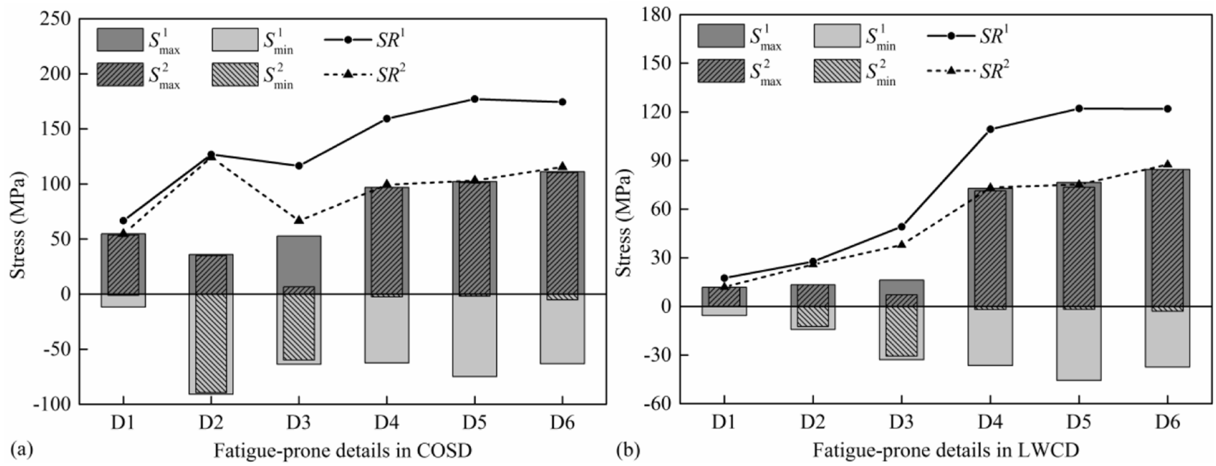

Fig. 10. Stress responses based on the influence surface method and three typical wheel loading paths.

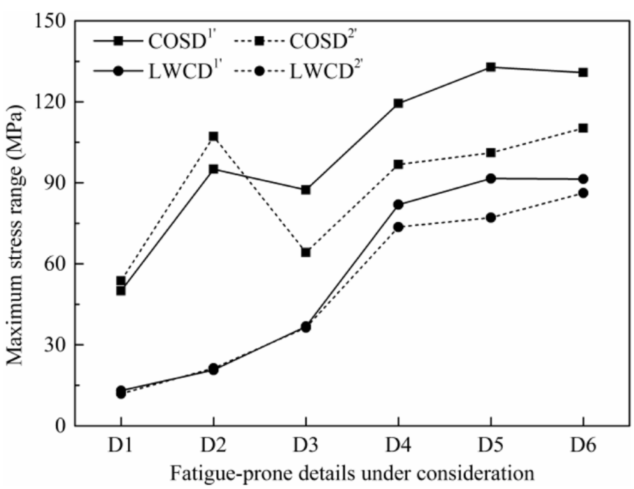

Fig. 11. Maximum stress ranges under Condition (1)' and Condition (2)'.

$$D = \sum_{S_i > \Delta\sigma_D} \frac{n_i \cdot S_i^{\beta}}{K_C} + \sum_{\Delta\sigma_D \geqslant S_j > \Delta\sigma_L} \frac{n_j \cdot S_j^{\beta+2}}{K_D} \tag{4}$$

where S_i and S_j are the stress ranges larger than $\Delta\sigma_D$ and between $\Delta\sigma_L$ and $\Delta\sigma_D$, respectively; n_i and n_j are the numbers of stress ranges of S_i and S_j, respectively; $\Delta\sigma_D$ and $\Delta\sigma_L$ are the CAFL and the cut-off limit of stress ranges, respectively, as listed in Table 1; β is the slope of the *S-N* curve, adopting a value of 3 for the high-stress range; and K_C and K_D are the fatigue strength coefficients corresponding to high-stress ranges and low-stress ranges, respectively, which can be determined based on the *S-N* curve specified in the Chinese code [38] and the Eurocode 3 [25]. Specifically, the accumulated fatigue damage of the fatigue-prone detail reaches the critical value of 1 after experiencing 2×10^6 stress cycles with a stress range of $\Delta\sigma_C$. Based on Eq. (4), the value of K_C can be calculated as follows:

$$K_C = \frac{\sum n_i \cdot S_i^{\beta}}{D} = 2 \times 10^6 \cdot (\Delta\sigma_C)^{\beta} \tag{5}$$

Similarly, the value of K_D can also be determined. It should be noted that the limitations of using the *S-N* curve and Miner's methods for fatigue analysis were not considered in this study [41].

As the transverse location of vehicles can significantly affect the fatigue evaluation of OSDs [12,28], multi-path models are adopted in many bridge codes, including the British Standard [29] and Eurocode 1 [21], to modify the stress range to consider the effect of the transverse

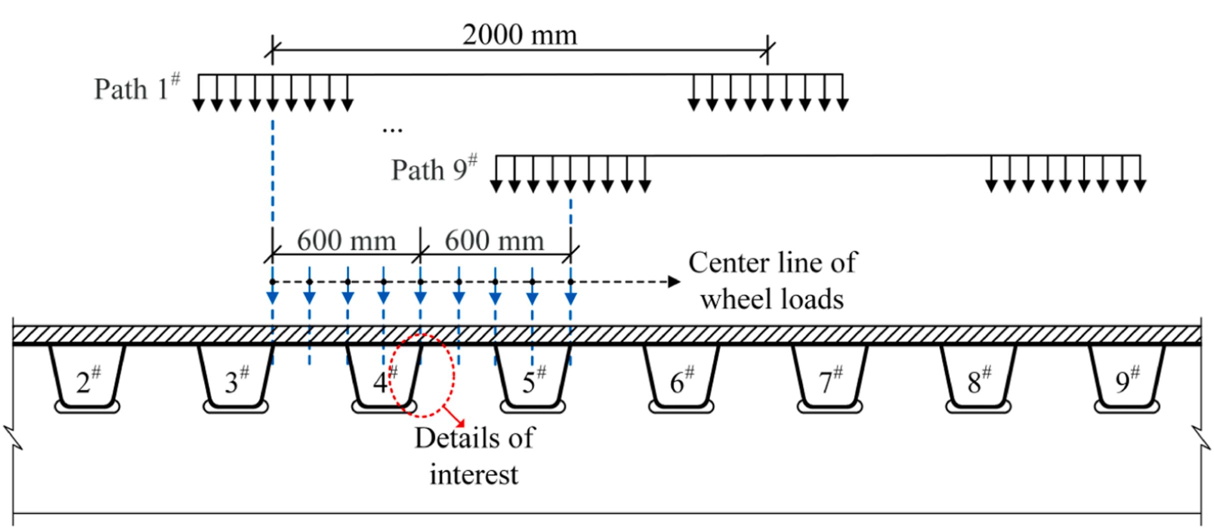

Fig. 12. Illustration of the proposed loading scheme.

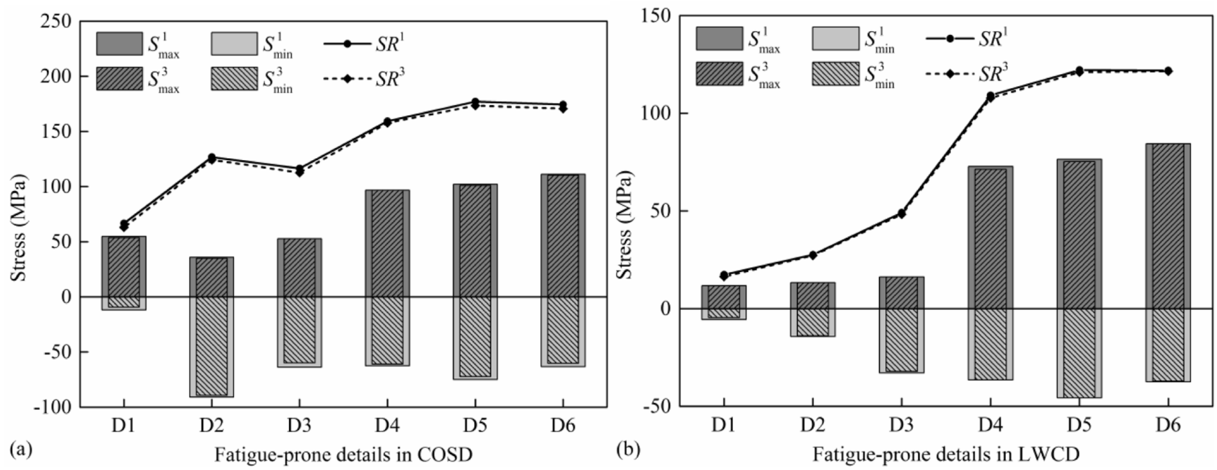

Fig. 13. Stress responses based on the influence surface method and proposed loading scheme.

position of vehicles on the fatigue evaluation of OSDs. The conventional procedures can be described as follows: (1) the stress influence surface of the concerned fatigue-prone detail is obtained through FE analysis; (2) the transverse location of fatigue design loads inducing the most unfavorable stress of the fatigue-prone detail is determined; (3) the most unfavorable location of fatigue design loads is taken as the center of the distribution of wheel loads, and then the modified stress range can be calculated according to the probability of vehicles passing the bridge deck from each transverse location under consideration, as illustrated in Fig. 14.

Considering that the number of stress cycles may also be affected by the transverse location of vehicles [28], an equivalent stress range (ESR) considering both the number and magnitude of stress ranges was defined in this paper for the convenience of calculation and analysis, which is expressed in Eq. (6).

$$\mathrm{ESR} = \left[\sum\left(n_i \cdot S_i^{\beta}\right) + (\Delta\sigma_D)^{-2} \cdot \sum\left(n_j \cdot S_j^{\beta+2}\right)\right]^{1/\beta} \tag{6}$$

Then, the modified ESR (denoted as MESR) induced by a single truck, considering the effect of the transverse location of vehicles, can be calculated as follows:

$$\mathrm{MESR} = \sqrt[\beta]{\sum\left(P_k \cdot \mathrm{ESR}_k^{\beta}\right)} \tag{7}$$

where P_k is the frequency of trucks passing from the transverse location k; and ESR_k is the ESR induced by a single fatigue design truck applied along the transverse location k.

Substituting Eq. (6) and Eq. (7) into Eq. (4), the modified fatigue damage induced by a single truck can be calculated as follows:

$$D_S = \frac{\mathrm{MESR}^{\beta}}{K_C} \tag{8}$$

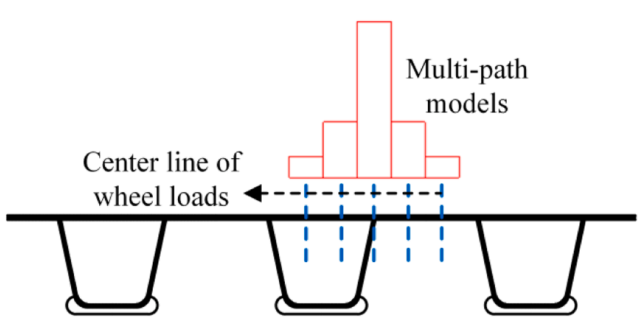

Fig. 14. Illustration of considering the distribution of transverse locations of vehicles.

Then, the fatigue life can be evaluated as follows:

$$Y = \frac{1}{365 \cdot N_T \cdot D_S} \tag{9}$$

where N_T is the average daily truck traffic in a lane.

As the stress ranges of critical fatigue-prone details induced by the fatigue design load applied along different transverse locations in Eq. (7) are generally determined separately, stress reversals generated by vehicles passing the bridge in sequence from different transverse locations have been ignored. As a result, the MESR of fatigue-prone details may be underestimated, resulting in an overestimated fatigue life. To consider the effect of stress reversals on the result of MESR, the calculation procedures were developed as follows: (1) based on FE analysis, the most unfavorable transverse location was determined using the proposed wheel loading paths (Fig. 12) and was taken as the center of the distribution of wheel loads; (2) a single fatigue design truck was applied separately along each concerned transverse location to extract the corresponding stress histories of fatigue-prone details under consideration; (3) a vector of transverse locations for N fatigue design trucks was randomly generated based on the frequency distribution under consideration; (4) by sequentially splicing the extracted stress history induced by each truck passing from the corresponding transverse location in the vector, a completed stress history of the considered fatigue-prone detail induced by N fatigue design trucks can be obtained; (5) the stress range spectrum was obtained through the rainflow counting method [42], and then the MESR considering the effect of stress reversals was calculated as Eq. (10); (6) Steps (3) - (5) was repeatedly carried out for 20 times, and the average value of MESRs was obtained for analysis after adjusting the value of N to make the discreteness of MESRs meet the requirements. The flowchart for the calculation procedure is shown in Fig. 15.

$$\mathrm{MESR} = \left[\frac{\sum\left(n_{i,N} \cdot S_{i,N}^{\beta}\right) + (\Delta\sigma_D)^{-2} \cdot \sum\left(n_{j,N} \cdot S_{j,N}^{\beta+2}\right)}{N}\right]^{1/\beta} \tag{10}$$

where N is the number of fatigue design trucks used in the calculation procedures; and $n_{i,N}$ and $n_{j,N}$ are the numbers of stress ranges of $S_{i,N}$ ($S_{i,N} > \Delta\sigma_D$)and $S_{j,N}$ ($\Delta\sigma_D \geq S_{j,N} > \Delta\sigma_L$), respectively, which are induced by the N fatigue design trucks.

It should be noted that the maximum tensile and compressive stresses of each fatigue-prone detail are induced by wheel loads applied in different transverse locations. Besides, the frequency distribution of vehicle transverse locations varies in different regions, which may also affect the fatigue life evaluation [28]. Therefore, four distribution patterns of vehicle transverse locations (i.e., Distribution A, B, C, and D, as illustrated in Fig. 16) were considered to investigate the effect of stress reversals on the MESR and thus on the finite fatigue life evaluation. In

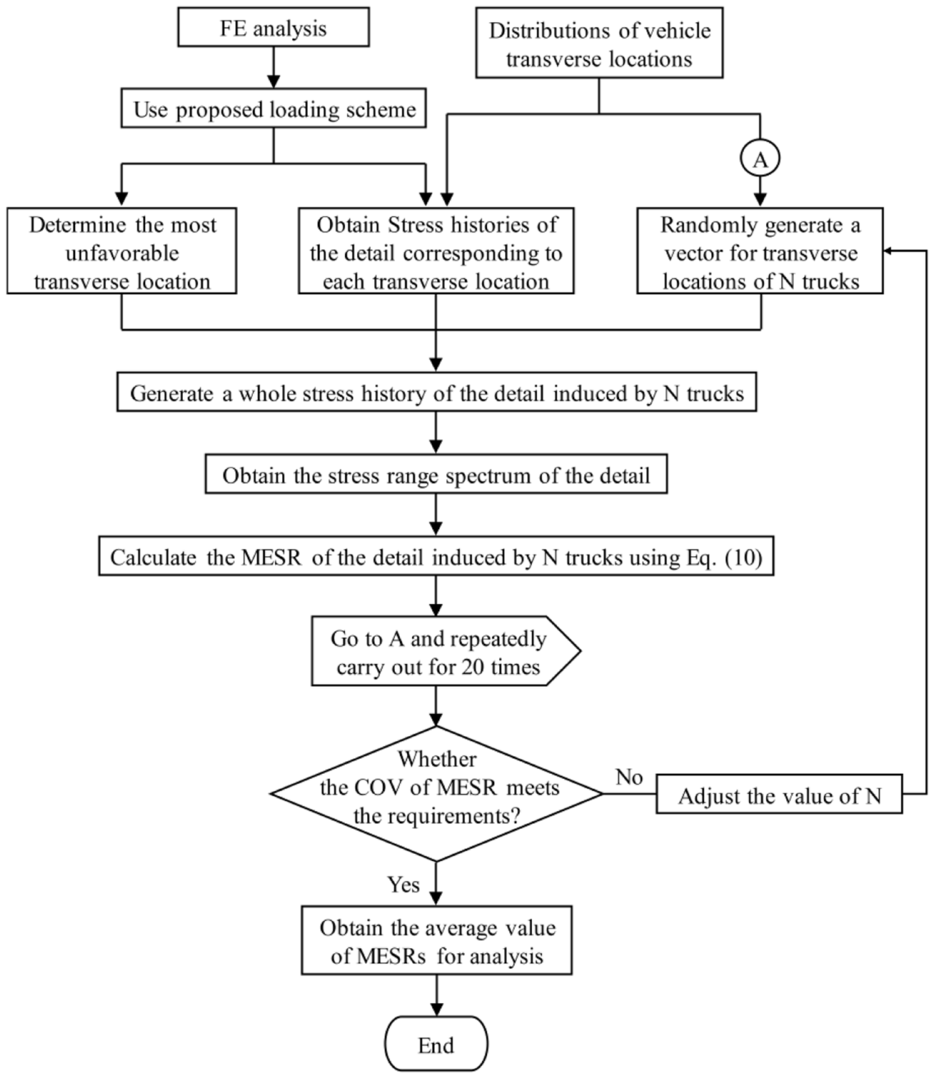

Fig. 15. Calculation flowchart of MESR considering the effect of stress reversals.

the analysis, Distribution A is recommended by Eurocode 1 [21], Distribution B is recommended by the British code (BS 5400) [29], Distribution C was measured at the Humen Bridge in China by Cui et al. [39], and Distribution D was proposed by Getachew A [40] based on the data of the measured transverse location of heavy trucks.

Fig. 17 illustrates a segment of the stress history of detail D3 in the COSD obtained through the calculation procedures considering the effect of stress reversals under Distribution C. The influence of the randomness of vehicle transverse locations on the calculation result of MESR of the concerned fatigue-prone details is shown in Fig. 18, from which it can be seen that 1×10^4 trucks are sufficient to achieve a satisfying result with a variation coefficient of less than 0.005. Therefore, N was set as 1×10^4 in this paper.

The MESRs of fatigue-prone details under consideration in the COSD and the LWCD were obtained under two conditions, i.e., Condition a and Condition b, in which four distribution patterns of vehicle transverse locations were considered. Condition a does not consider the effect of stress reversals on the MESR (denoted as MESR^a), while Condition b considers the effect of stress reversals on the MESR (denoted as MESR^b). The obtained MESRs of the fatigue-prone details under the two conditions are shown in Fig. 19. It should be pointed out that details D1, D2, and D3 in the LWCD were not included in the discussion in this section because details D1 and D2 meet the requirement for infinite fatigue life, while most of the stress ranges of detail D3 are lower than the cut-off limit and may result in unrepresentative results. It can be observed from Fig. 19 that the MESR^b of each fatigue-prone detail in both the COSD and the LWCD is much greater than the MESR^a obtained under the same distribution of vehicle transverse locations, which demonstrates the significant effect of stress reversals on the calculation of MESR of fatigue-prone details and thus on the evaluation of fatigue life of OSDs. Besides, it can be observed from Fig. 19 that the MESRs of these fatigue-prone details calculated under different distributions are quite different, and the difference between the MESRs calculated under Distribution A and Distribution D can even be more than 25.0 MPa, which indicates that the MESR can also be greatly affected by the distribution pattern of transverse location of vehicles. Specifically, the MESR^b of most fatigue-prone details calculated under different distributions is larger than the MESR^a calculated under Distribution B, indicating that the distribution of vehicle transverse locations recommended by BS 5400 [29] could be unsafe for the fatigue design or evaluation of OSDs when the effect of stress reversals is ignored. On the contrary, the MESR^{b}s of details D1, D2, and D3 in the COSD calculated under Distribution A are considerably greater than those obtained under other distributions. These results indicate that using an inappropriate distribution of vehicle transverse locations may result in unsafe or over-conservative fatigue life evaluation results, while ignoring the effect of stress reversals may lead to an underestimation of vehicle load effect and then an overestimated fatigue life. Therefore, it is better to obtain the transverse distribution pattern of

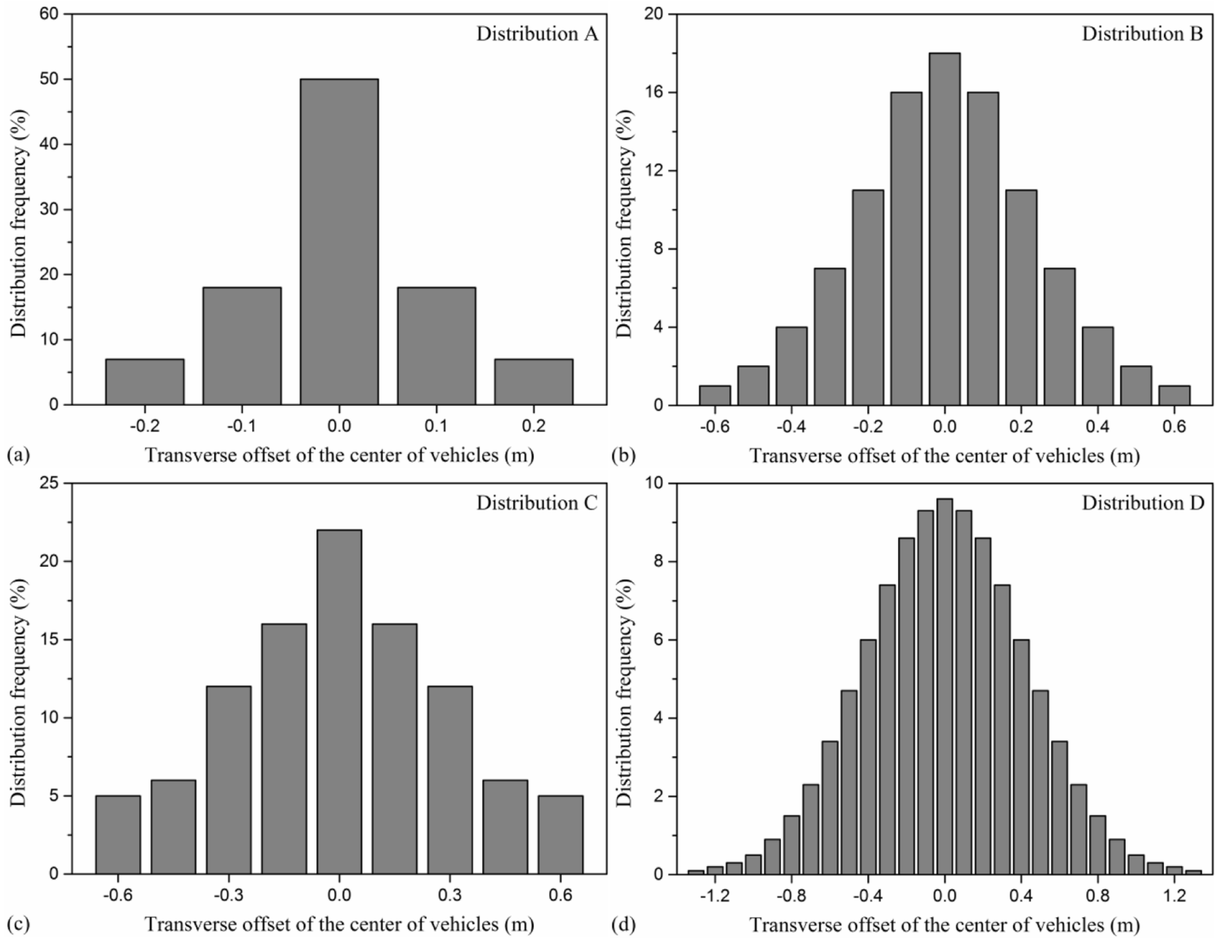

Fig. 16. Frequency distributions of vehicle transverse locations under consideration.

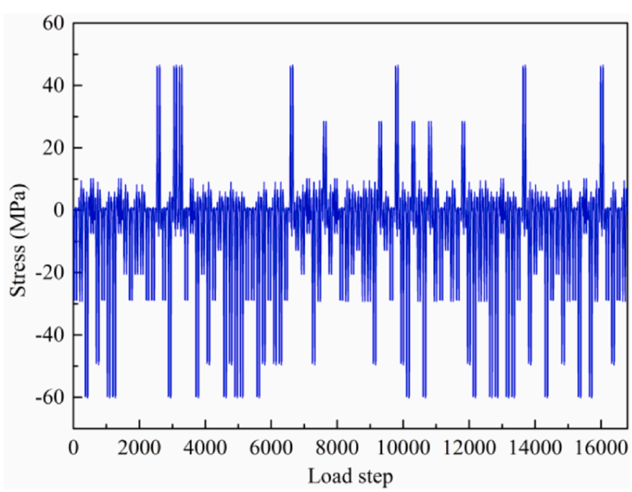

Fig. 17. Simulative stress history of detail D3 in the COSD.

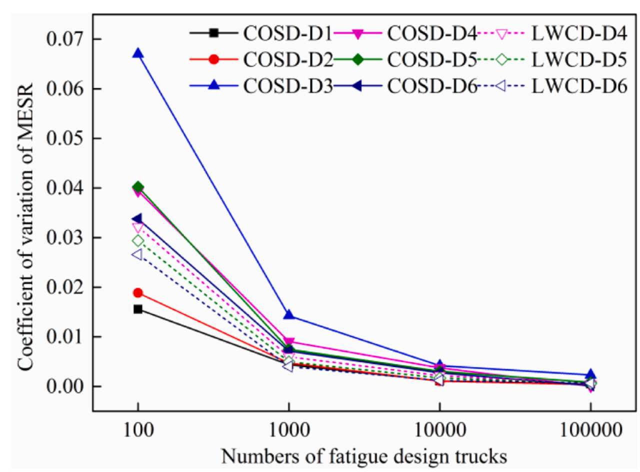

Fig. 18. Coefficient of variations of MESR.

vehicles according to the local traffic data and Distribution B is recommended for fatigue design when the local traffic data is not available. In addition, comparing the results in Fig. 19**(a)** and Fig. 19**(b)**, it can be found that the MESR of fatigue-prone details in the LWCD is much less than that in the COSD under the same condition. For example, the MESR^b of detail D6 in the LWCD under Distribution B is 82.8 MPa, which is 22.7% lower than that of the COSD (107.2 MPa). It indicates that the LWCD can significantly reduce the stress response of fatigue-prone details and thus effectively prolong the fatigue life of OSDs.

To quantify the effect of stress reversals on the finite fatigue life evaluation of OSDs, ratios of fatigue lives (Y^a) of the fatigue-prone details in the COSD and the LWCD obtained under Condition a to those (Y^b) obtained under Condition b, namely Y^a/Y^b, were calculated under four distribution patterns of vehicle transverse locations based on Eq. (9), as shown in Fig. 20. It can be observed from Fig. 20 that the effect of the distribution pattern of vehicle transverse locations on the ratios of Y^a to Y^b is significant. When Distribution A is taken into account, the ratios of

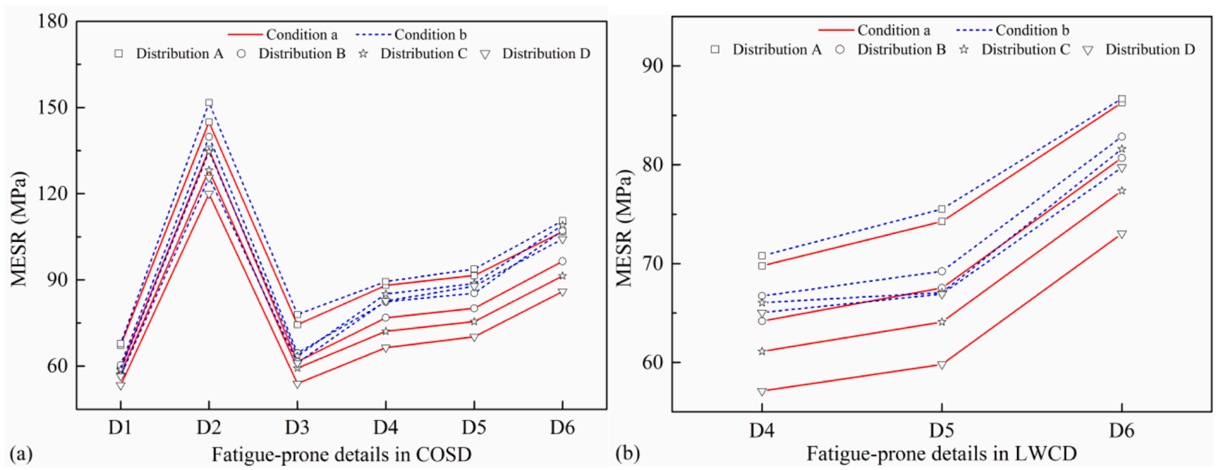

Fig. 19. MESRs under different conditions and distributions.

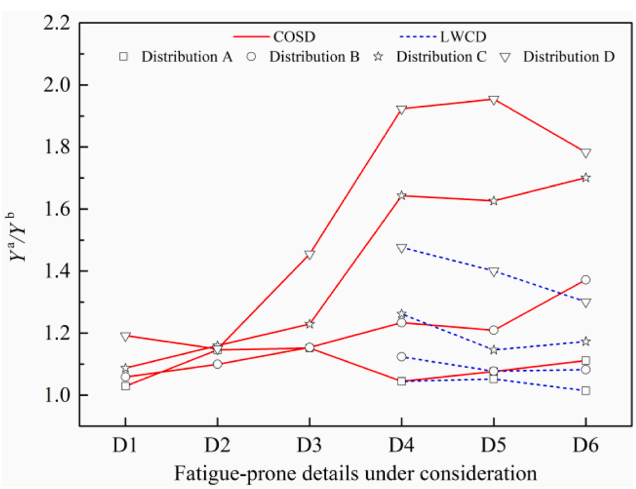

Fig. 20. Ratios of Y^a to Y^b.

most fatigue-prone details in the COSD and the LWCD are slightly larger than 1.0, which means that the stress reversals under Distribution A have little effect on the MESR and thus on the fatigue life of fatigue-prone details. This may be due to the fact that the maximum transverse offset of the vehicle under Distribution A is only 0.2 m, resulting in the fatigue-prone details experiencing few stress reversals. However, the ratio can be much greater than 1.0 under other distributions. In particular, the ratio of detail D5 in the COSD under Distribution D even reaches 1.95, indicating that the fatigue life of the COSD evaluated under Distribution D may be overestimated by 95% if the stress reversals are ignored. Besides, as shown in Fig. 20, the ratio of each fatigue-prone detail in the LWCD is much less than that in the COSD, which means that the effect of stress reversals on the finite fatigue life evaluation of the LWCD is much less than that of the COSD. This may be due to the fact that the UHPC layer can improve the local stiffness of the bridge deck system and thus the wheel loads can be more evenly-distributed before being transferred to the bridge deck.

Considering overloading has become an increasingly prevalent phenomenon in bridge engineering [43], the influence of stress reversals on the fatigue life evaluation under the condition of overloading was also investigated using the above analysis procedure. Four overloading rates were considered, including 10%, 20%, 30%, and 40%, and the corresponding gross weights of overloaded vehicles are 528 kN, 576 kN, 624 kN, and 672 kN, respectively. It should be noted that the load was evenly distributed to each axis of the vehicle model and the violation rate of overloaded vehicles was not considered. Ratios of fatigue lives (Y_{D}) of fatigue-prone details in the COSD and the LWCD evaluated based on the measured truck traffic (Distribution D) with different overloading ratios to those (Y_{D}) evaluated based on the fatigue design load (Distribution A) were calculated under Condition a and Condition b, namely Y_D^a/Y_A^a andY_D^b/Y_A^b, as illustrated in Fig. 21. When the ratio is greater than 1.0, it means that the fatigue-prone detail designed based on the fatigue design load is unsafe. It can be seen from Fig. 21 that as the overloading ratio increases, both the ratios of Y_D^a/Y_A^a and Y_D^b/Y_A^b increase, but the increase rate of the former is much smaller than the latter. In particular, the required overloading ratio for the ratios of $Y_{\mathrm{D}}/Y_{\mathrm{A}}$ of most fatigue-prone details to reach around 1.0 decreases from 30% under Condition a to 10% under Condition b. This indicates that the stress reversals induced by overloaded trucks tend to have a more significant effect on the finite fatigue life evaluation of OSD systems. Hence, the fatigue life of OSDs could be overestimated if the stress reversals induced by overloaded trucks are ignored, which would lead to inappropriate fatigue designs or maintenance of OSDs.

6. Conclusions

In this paper, numerical simulations were conducted to study the fatigue life evaluation of OSDs considering the effect of stress reversals induced by vehicles passing the bridge deck in sequence from different transverse locations. FE models of two typical OSD systems, i.e., the COSD and the LWCD, were developed, and the stress responses of six typical fatigue-prone details under the action of vehicles were obtained. To study the effect of stress reversals on the infinite fatigue life evaluation of OSDs, the maximum stress range of fatigue-prone details under consideration was analyzed based on the stress influence surface method and the commonly-used simplified loading method using three typical wheel paths. To investigate the effect of stress reversals on the finite fatigue life evaluation of OSDs, the modified equivalent stress ranges and fatigue lives of fatigue-prone details under consideration were calculated and compared, in which a variety of distribution patterns of vehicle transverse locations and overloading rates were considered. Based on the above investigation, the conclusions can be summarized as follows:

(1) The most unfavorable stress reversal can be generated by vehicles traveling from two critical transverse locations in the same traffic lane. Three typical wheel paths can only be used to determine the most unfavorable stress of fatigue-prone details in OSDs induced by vehicle loads, but cannot be used to determine the maximum stress range, which may result in an underestimation of the maximum stress range by 40% or more and thus leads to

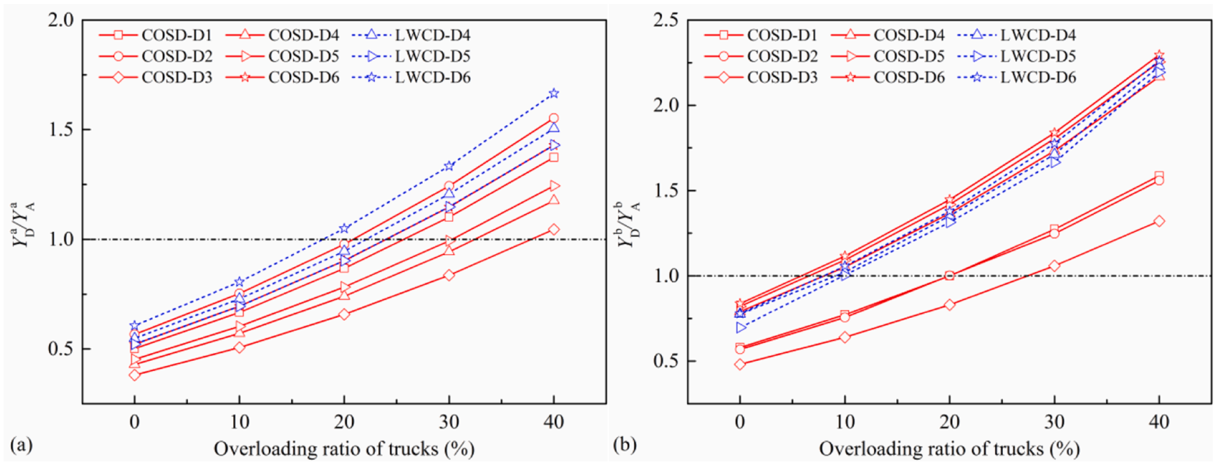

Fig. 21. Ratios of Y_D^a/Y_A^a andY_D^b/Y_A^b.

inaccurate results of the infinite fatigue life evaluation of both the COSD and the LWCD.

(2) A convenient and efficient vehicle loading scheme was proposed to accurately capture both the maximum and minimum stresses of critical fatigue-prone details in OSDs under the action of vehicle loads, based on which the error of the obtained maximum stress range can be less than 3%.

(3) The stress reversals induced by vehicles traveling with different distributions of transverse locations can significantly affect the finite fatigue life evaluation of OSD systems. Specifically, the fatigue life of OSDs could be overestimated by 95% if stress reversals are ignored. Besides, the stress reversals induced by overloaded trucks have a significant effect on the fatigue performance of OSDs.

(4) The effect of stress reversals on the finite fatigue life evaluation of the LWCD, as well as the stress responses of fatigue-prone details in the LWCD, are much less than those of the COSD, which indicates a better anti-fatigue performance of the LWCD over the COSD.

CRediT authorship contribution statement

Shengquan Zou: Conceptualization, Methodology, Software, Formal analysis, Investigation, Writing – original draft. **Ran Cao:** Validation, Writing – review & editing, Data curation, Supervision. **Lu Deng:** Resources, Writing – review & editing, Supervision, Project administration, Funding acquisition. **Wei Wang:** Investigation, Writing – review & editing, Formal analysis, Visualization.

Declaration of Competing Interest

The authors declare that they have no known competing financial interests or personal relationships that could have appeared to influence the work reported in this paper.

Acknowledgments

This work was supported by the National Natural Science Foundation of China (Grant No. 51778222); the Key Research Project of Hunan Province (Grant No. 2017SK2224); and the Hunan Province funding for leading scientific and technological innovation talents (Grant No. 2021RC4025).

References

[1] Kolstein MH. Fatigue classification of welded joints in orthotropic steel bridge decks. The Netherlands: Delft University of Technology; 2007 [Ph.D Thesis].

[2] Ya S, Yamada K, Ishikawa T. Fatigue evaluation of rib-to-deck welded joints of orthotropic steel bridge deck. J Bridge Eng 2011;16(4):492–9. https://doi.org/10.1061/(ASCE)BE.1943-5592.0000181.

[3] Yan F, Chen WZ, Lin ZB. Prediction of fatigue life of welded details in cable-stayed orthotropic steel deck bridges. Eng Struct 2016;127:344–58. https://doi.org/10.1016/j.engstruct.2016.08.055.

[4] Wolchuk R. Lessons from weld cracks in orthotropic decks on three European bridges. J Struct Eng 1990;116(1):75–84. https://doi.org/10.1061/(ASCE)0733-9445(1990)116:1(75).

[5] Sim HB, Uang CM. Stress analyses and parametric study on full-scale fatigue tests of rib-to-deck welded joints in steel orthotropic decks. J Bridge Eng 2012;17(5): 765–73. https://doi.org/10.1061/(ASCE)BE.1943-5592.0000307.

[6] Zhang QH, BU YZ, LI Qiao. Review on fatigue problems of orthotropic steel bridge deck. China Journal of Highway and Transport 2017;30.3:14-30. https://doi.org/10.19721/j.cnki.1001-7372.2017.03.002. (in Chinese).

[7] De Jong FBP, Boersma PD. Lifetime calculations for orthotropic steel bridge decks. The 10th international conference and exhibition-structural faults and repair conference. London; 2003.

[8] Xiao ZG, Yamada K, Inoue J, Yamaguchi K. Fatigue cracks in longitudinal ribs of steel orthotropic deck. Int J Fatigue 2006;28(4):409–16. https://doi.org/10.1016/j.ijfatigue.2005.07.017.

[9] Guo T, Li AQ, Li JH. Fatigue life prediction of welded joints in orthotropic steel decks considering temperature effect and increasing traffic flow. Struct Health Monit 2008;7(3):189–202. https://doi.org/10.1177/1475921708090556.

[10] Shao XD, Yi DT, Huang ZY, Zhao H, Chen B, Liu ML. Basic performance of the composite deck system composed of orthotropic steel deck and ultrathin RPC layer. J Bridge Eng 2013;18(5):417–28. https://doi.org/10.1061/(ASCE)BE.1943-5592.0000348.

[11] Graybeal B, Brühwiler E, Kim BS, Toutlemonde F, Voo YL, Zaghi A. International perspective on UHPC in bridge engineering. J Bridge Eng 2020;25(11). https://doi.org/10.1061/(ASCE)BE.1943-5592.0001630. 04020094.

[12] Xiao ZG, Yamada K, Ya S, Zhao XL. Stress analyses and fatigue evaluation of rib-to-deck joints in steel orthotropic decks. Int J Fatigue 2008;30(8):1387–97. https://doi.org/10.1016/j.ijfatigue.2007.10.008.

[13] Kim YC, Hirohata M, Shibata K, Chang KH. Detection and monitoring by FSM for fatigue crack at invisible location of steel plate deck with U-rib. Int J Steel Struct 2013;13(1):183–9. https://doi.org/10.1007/s13296-013-1017-6.

[14] Cui C, Bu YZ, Bao Y, Zhang QH, Ye ZT. Strain energy-based fatigue life evaluation of deck-to-rib welded joints in OSD considering combined effects of stochastic traffic load and welded residual stress. J Bridge Eng 2018;23(2):04017127. https://doi.org/10.1061/(ASCE)BE.1943-5592.0001181.

[15] Connor RJ. Manual for design, construction, and maintenance of orthotropic steel deck bridges. Report No. FHWA-IF-12-027. United States: Federal Highway Administration; 2012. http://www.fhwa.dot.gov/bridge/pubs/if12027/if12027.pdf.

[16] Hobbacher A. Recommendations for fatigue design of welded joints and components. 2nd ed. Cham: Springer International Publishing; 2016.

[17] De Jong FBP. Overview fatigue phenomenon in orthotropic bridge decks in the Netherlands. 2004 Orthotropic bridge conference. Sacramento; 2004.

[18] Zhu Z, Xiang Z, Zhou YE. Fatigue behavior of orthotropic steel bridge stiffened with ultra-high performance concrete layer. J Constr Steel Res 2019;157:132–42. https://doi.org/10.1016/j.jcsr.2019.02.025.

[19] Connor RJ, Fisher JW. Results of field measurements on the Williamsburg Bridge orthotropic deck: Final report on Phase III. ATLSS Engineering Research Center, Lehigh Univ.; 2001.

[20] ECS (European Committee for Standardization). Eurocode 3: Design of steel structures — Part 2: Steel bridge. Brussels (Belgium): EN 1993-2:2006;2006.
[21] ECS (European Committee for Standardization). Eurocode 1: Actions on structure — Part 2: Traffic loads on bridges. Brussels (Belgium): EN 1991-2:2003;2003.
[22] Zhang SH, Shao XD, Cao JH, Cui JF, Hu JH, Deng L. Fatigue performance of a lightweight composite bridge deck with open ribs. J Bridge Eng 2016;21(7): 04016039. https://doi.org/10.1061/(ASCE)BE.1943-5592.0000905.
[23] Zhu ZW, Yuan T, Xiang Z, Huang Y, Zhou YE, Shao XD. Behavior and fatigue performance of details in an orthotropic steel bridge with UHPC-deck plate composite system under in-service traffic flows. J Bridge Eng 2018;23(3): 04017142. https://doi.org/10.1061/(ASCE)BE.1943-5592.0001167.
[24] Li LF, Zeng Y, Pei BD, Wang LH. Stress characteristic analysis and field test on the cutouts of light-weight composite deck. China J Highway. in Chinese Transport 2019;32(8):66–78. https://doi.org/10.19721/j.cnki.1001-7372.2019.08.006.
[25] ECS (European Committee for Standardization). Eurocode 3: Design of steel structures—Part 1-9: Fatigue. Brussels (Belgium): EN 1993-1-9:2005;2005.
[26] Miner MA. Cumulative damage in fatigue. J Appl Mech 1945;12(3). A159–A164.
[27] Ya S, Yamada K. Fatigue durability evaluation of trough to deck plate welded joint of orthotropic steel deck. Doboku Gakkai Ronbunshuu A 2008;64(3):603–16. https://doi.org/10.2208/jsceja.64.603.
[28] Zhou XY, Treacy M, Schmidt F, Brühwiler E, Toutlemonde F, Jacob B. Effect on bridge load effects of vehicle transverse in-lane position: A case study. J Bridge Eng 2015;20(12):04015020. https://doi.org/10.1061/(ASCE)BE.1943-5592.0000763.
[29] BSI (British Standards Institution), Steel, concrete and composite bridges — Part 10: Code of practice for fatigue. BS 5400: Part 10;1980.
[30] Maljaars J, van Dooren F, Kolstein H. Fatigue assessment for deck plates in orthotropic bridge decks. Steel Constr 2012;5(2):93–100. https://doi.org/10.1002/stco.201210011.
[31] Shao XD, Qu WT, Cao JH, Yao YL. Static and fatigue properties of the steel-UHPC lightweight composite bridge deck with large U ribs. J Constr Steel Res 2018;148: 491–507. https://doi.org/10.1016/j.jcsr.2018.05.011.
[32] Luo J, Shao X, Cao J, Xiong M, Fan W. Transverse bending behavior of the steel-UHPC lightweight composite deck: Orthogonal test and analysis. J Constr Steel Res 2019;162:105708. https://doi.org/10.1016/j.jcsr.2019.105708.
[33] Wang Y, Li ZX, Li AQ. Combined use of SHMS and finite element strain data for assessing the fatigue reliability index of girder components in long-span cable-stayed bridge. Theor Appl Fract Mec 2010;54(2):127–36. https://doi.org/10.1016/j.tafmec.2010.10.008.
[34] AASHTO. AASHTO LRFD bridge design specifications. 6th ed. Washington, D.C.: AASHTO; 2017.
[35] Poutiainen I, Tanskanen P, Marquis G. Finite element methods for structural hot spot stress determination—a comparison of procedures. Int J Fatigue 2004;26(11): 1147–57. https://doi.org/10.1016/j.ijfatigue.2004.04.003.
[36] Cao J, Shao X, Deng Lu, Gan Y. Static and fatigue behavior of short-headed studs embedded in a thin ultrahigh-performance concrete layer. J Bridge Eng 2017;22 (5):04017005. https://doi.org/10.1061/(ASCE)BE.1943-5592.0001031.
[37] Xiao ZG, Yamada K. A method of determining geometric stress for fatigue strength evaluation of steel welded joints. Int J Fatigue 2004;26(12):1277–93. https://doi.org/10.1016/j.ijfatigue.2004.05.001.
[38] MPTRC (Ministry of Transport of the People's Republic of China). Specifications for design of highway steel bridge. Beijing: People Communications Press;2015. (in Chinese).
[39] Cui B, Wu C, Ding WJ, Tong YQ. Influence of acting position of vehicle wheels on fatigue stress range of steel deck. in Chinese J Architecture Civil Eng 2010;27(3): 19–23. https://doi.org/10.19815/j.jace.2010.03.004.
[40] Getachew A. Traffic load effects on bridges, statistical analysis of collected and Monte Carlo simulated vehicle data. Sweden: Royal Institute of Technology; 2003 [Ph.D Thesis].
[41] Ye XW, Su YH, Han JP. A state-of-the-art review on fatigue life assessment of steel bridges. Mathematical Problems in Engineering 2014;2014:1–13. https://doi.org/10.1155/2014/956473.
[42] Matsuishi M, Endo T. Fatigue of metals subjected to varying stress. Japan Society of Mechanical Engineers. Japan (Fukuoka):68(2),37-40;1968.
[43] Yan WC, Deng L, Zhang F, Li TG, Li SF. Probabilistic machine learning approach to bridge fatigue failure analysis due to vehicular overloading. Eng Struct 2019;193: 91–9. https://doi.org/10.1016/j.engstruct.2019.05.028.